

# Graded-index optical fiber emulator of an interacting three-atom system: Classical non-separability and illumination control of particle statistics

M.A. Garcia-March,<sup>1</sup> N.L. Harshman,<sup>2</sup> H. da Silva,<sup>3</sup> T. Fogarty,<sup>4</sup> Th. Busch,<sup>4</sup> M. Lewenstein,<sup>1,5</sup> and A. Ferrando<sup>6</sup>

<sup>1</sup>*ICFO – Institut de Ciències Fotoniques, The Barcelona Institute of Science and Technology, Av. Carl Friedrich Gauss 3, 08860 Castelldefels (Barcelona), Spain*

<sup>2</sup>*Department of Physics, American University, 4000 Massachusetts Avenue NW, Washington, DC 20016, USA*

<sup>3</sup>*Universidade Federal de Itajubá, Av. BPS 1303, Itajubá, Minas Gerais 37500-903, Brazil*

<sup>4</sup>*Quantum Systems Unit, Okinawa Institute of Science and Technology Graduate University, 1919-1 Tancha, Onna, Okinawa 904-0495, Japan*

<sup>5</sup>*ICREA, Pg. Lluis Companys 23, 08010 Barcelona, Spain*

<sup>6</sup>*Department d'Òptica. Universitat de València, Dr. Moliner, 50, E-46100 Burjassot (València), Spain*

We show that optical fibers with a graded-index profile and thin metallic slabs can be used to emulate a system of three ultracold strongly interacting atoms. We study the symmetries present in the eigenstates by using discrete group theory, always comparing our results with those previously found from the atomic physics approach. The symmetry analysis allows us to prove that, by spatially modulating the incident field, one can select the atomic statistics, i.e., emulate a system of three bosons, fermions or two bosons or fermions plus an additional distinguishable particle. We show that the optical system is able to produce classical non-separability resembling that found in the analogous atomic system.

## I. INTRODUCTION

A fruitful mental strategy is to compare two different systems, a source and a target. Similarities guide deduction and allow one to learn how the target system works. This tool is commonly called an *analogy*. The concept of analogy has modified its meaning since its initial Greek inception as a proportion between two sets. Logicians call an *argument from analogy* a deduction through which one uses an analogy to infer a property for the target system: one first finds a set of properties shared between source and target, and henceforth tries to investigate if a property of the source, which is not yet found in the target, occurs in the target system. The history of physics is full of successful (and unfortunate) examples of the use of an analogy; for example, see Ref. [1] for a beautiful compendium of how acoustics was a source of inspiration for physicists such as Newton, Faraday and Young.

Here we set an analogy between the target system, a graded-index (GRIN) optical fiber with three thin slabs of a metallic material in an hexagonal geometry (see Fig. 1), and the source, a quantum system of three atoms interacting through a strong, short-range potential. We consider the paraxial propagation of a polarized monochromatic laser beam in such a fiber. The wave propagation equation is Schrödinger-like and often called the Fock-Leontovich equation [2, 3]. The longitudinal dimension along the fiber plays the role of time and the inhomogeneous refractive index profile of the fiber plays the role of the external potential. In our proposal the GRIN modulation of the refractive index is the analogue of a parabolic trap potential for the three atoms and we will show that the thin metallic slabs can play the role of the contact interactions between the atoms. By properly designing the spatial profile of the incident laser beam we show that it is possible to produce an analogous sys-

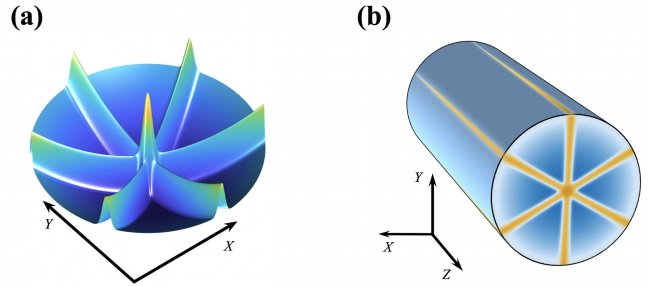


FIG. 1. Schematic of the system. (a) Representation of the refractive index in the  $x-y$  plane. (b) Schematic of the fiber.

tem to three identical atoms. The profile of the incident beam allows for the selection of the statistics of the atoms emulated, that is, if they resemble bosons, fermions, or mixtures. This system is one of the first systems that represent an analogy between optics and *interacting* quantum systems; see [4] for an experiment on an interacting system in a different set up.

Our model is a new example of an analogy between a classical and a quantum system, a well-known productive strategy in modern science [5]. More particularly, it is an example of a quantum-optical analogy, within a photonic structure, which highlights the wave nature of both disciplines [6–8]. An inferred property for the target optical system from the source quantum system is the existence of classical entanglement [9–11]. Classical entanglement occurs in a wide variety in optical systems, is not restricted to those described by the Fock-Leontovich equation, and often includes polarization degrees of freedom [12]. In general it requires a vectorial nature of the wave [13]. It has been proposed that a better name is to call this property *classical non-separability* [14] because the target system lacks the non-locality property

of quantum systems with entanglement [13]. Here we mean the non-locality associated with a measurement of an entangled system, which when taken in one region of space, dictates the outcome in another region. In this sense, it has been clarified that there are two types of entanglement [9, 10, 12, 15]: i) intersystem entanglement (or true-multiparticle entanglement) and ii) intrasystem entanglement (between different degrees of freedom of a single particle). It is commonly accepted that intersystem entanglement can only occur in quantum systems. This kind of entanglement may lead to non-locality. The examples on classical non-separability found in literature are mostly associated to two different degrees of freedom of the same particle, and remarkable realizations of the creation of classical non-separable states on three degrees of freedom, i.e., were done using path, polarization and transverse modes [16]. We show how, in the system we introduce here, classical non-separability between different particles occurs in a scalar system. In this sense it is an analogous of type (i) entanglement (intersystem). But still the measurement problem remains, so it does not lead to non-locality. We note that there is a set of works where the goal is to use classical fields to reproduce non-classical correlations between different measurements [17–20], including simulations of Bell-like inequalities [21, 22].

We emphasize here that the characterization of the many modes guided by the GRIN fiber with three thin metallic slabs is of interest in itself for the optics community, independently of the analogy with the quantum system of three atoms. Graded-index fibers are multimode fibers, that is, they can propagate many modes [23–25]. There is a recent revival in the interest in these kinds of fibers, which have been identified as very interesting systems when spatio-temporal non-linear effects are considered [26, 27]. A non-comprehensive list of recent works include the observation of optical solitons and soliton self-frequency lifting [28], generation of ultrashort pulses and even supercontinuum [29], or beam self-cleaning [30, 31]. The description of pulse propagation in these fibers is rather difficult, as it must include both the three spatial dimensions and time, and implies the non-linear dynamics of multiple co-propagating modes (see a simplified model in [32]). Indeed, GRIN fibers represent an ideal set-up for a variety of phenomena in complexity science, due to the collective dynamics associated to the cooperation of disorder, dissipation, and non-linearity [30]. Here we do not consider spatio-temporal dynamics nor non-linearities, as we detail later. However, the characterization of this multimode GRIN fiber with thin metallic slabs allows for including both non-linearity and spatio-temporal effects in the future, and therefore it represents an important result of the paper.

In section II we detail the characteristics of the fiber under study. We perform a full modal analysis of this new kind of fiber, classifying the modes according to the rotational discrete symmetry of the system. We build the analogy with the atomic system in section III and inter-

pret the wave function as giving information of the ordering of the particles. We discuss in section IV the non-separability of the classical states. In section V we discuss the possible applications and further developments of this system. In appendix A we include a discussion of the modes symmetries and their relationship with particle statistics. In appendix B we discuss the exact solutions of the system, which are of interest even purely on optical grounds. Finally, in appendix C we review the Bose-Fermi mapping theorem, which maps a system of interacting bosons in a system of ideal fermions, which is of utility in the main discussion.

## II. OPTICAL SYSTEM: GRIN FIBER WITH THREE THIN METALLIC SLABS

The paraxial propagation of a monochromatic optical beam of constant polarization along a fiber with an inhomogeneous refractive index profile is given by

$$-i2n_0k_0\frac{\partial}{\partial\tilde{z}}\tilde{\Phi} = [\nabla_t^2 + k_0^2(\tilde{n}^2(\tilde{x},\tilde{y}) - n_0^2)]\tilde{\Phi}, \quad (1)$$

where  $\tilde{z}$  is the axial coordinate of the fiber,  $\{\tilde{x},\tilde{y}\}$  are the transverse coordinates,  $\nabla_t^2$  is the Laplacian in the transverse coordinates,  $\tilde{n}^2(\tilde{x},\tilde{y})$  is the index of refraction profile with a reference value of  $n_0$ , and  $k_0$  is the wave number. To facilitate comparison with the Schrödinger equation, we remove the dimensions by dividing by  $-2n_0k_0^2$

$$i\frac{\partial}{\partial z}\Phi = \left(-\frac{1}{2}\nabla_{x,y}^2 + \Delta n(x,y)\right)\Phi, \quad (2)$$

where,  $\{x,y,z\}$  are the dimensionless coordinates  $x = k_0\sqrt{n_0}\tilde{x}$ ,  $y = k_0\sqrt{n_0}\tilde{y}$ ,  $z = k_0\tilde{z}$ ,  $\Phi(x,y,z) = \tilde{\Phi}(\tilde{x},\tilde{y},\tilde{z})$ ,  $n(x,y) = \tilde{n}(\tilde{x},\tilde{y})$  and

$$\Delta n(x,y) = [n_0^2 - n^2(x,y)]/2n_0. \quad (3)$$

When the refractive index profile remains close to the reference index  $n_0$ , (3) simplifies to  $\Delta n(x,y) \approx [n_0 - n(x,y)]$ .

The form of (2) parallels the two-dimensional time-dependent Schrödinger equation with  $z$  playing the role of time and  $\Delta n(x,y)$  the role of potential energy. Making the substitution  $\Phi(x,y,z) = \exp(-i\mu z)\phi(x,y)$  to separate the longitudinal and transverse coordinates, one can see that solving for the transverse optical modes  $\phi(x,y)$  and paraxial propagation constant  $\mu$  is equivalent to solving for the energy spectrum of a quantum Hamiltonian with two degrees of freedom

$$H\phi(x,y) \equiv \left(-\frac{1}{2}\nabla_{x,y}^2 + \Delta n(x,y)\right)\phi(x,y) = \mu\phi(x,y). \quad (4)$$

This analogy between fiber optics in the paraxial approximation and two-dimensional quantum mechanics is well-known (see e.g. [33]) – (2) is indeed sometimes called the

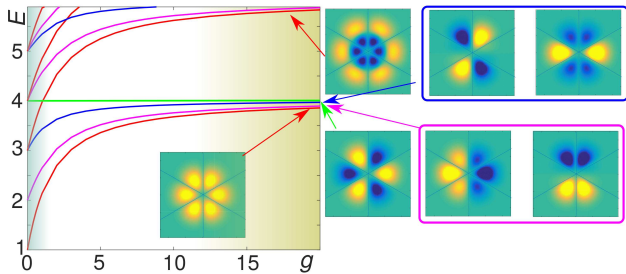


FIG. 2. Eigenenergies (propagation constant) for the optical Schrödinger equation (4) with  $\Delta n_{\text{tot}} = \Delta n_{\text{GRIN}} + \Delta n_{C_{6v}}$  plotted against varying barrier strength  $g$  for a fixed, narrow width  $\sigma$ . The shaded golden area highlights the region of large values of  $g$ , where the thin metallic slabs can be implemented with e.g. gold, as discussed in main text. The shaded green area highlights the region of low  $g$ , which has a weak  $\Delta n_{C_{6v}}$  refractive index that could be implemented with dielectric materials. Inset and to the right of the graph depicts the eigenmodes corresponding to the lowest seven modes (see Figs. 3 and 4). In all representations of the eigenmodes, the dotted lines indicate the position of the metallic slabs.

optical Schrödinger equation [34]. Here, we assume a longitudinally homogeneous fiber; relaxing this requirement allows the simulation of quantum systems with time-varying mass or potential.

We build our effective potential for the analogy by combining GRIN fibers with metallic sectioning. A GRIN fiber has a refractive index  $n(x, y)$  that decreases continuously with the radial distance to the optical axis of the fiber. Here we consider the particular case of a parabolic profile that focuses the beam and provides guidance in the fiber (also called selfoc fibers [3]), i.e.

$$\Delta n_{\text{GRIN}}(x, y) = \begin{cases} \frac{1}{2}(x^2 + y^2), & \text{if } \rho = \sqrt{x^2 + y^2} < R \\ \frac{1}{2}R^2, & \text{if } \rho = \sqrt{x^2 + y^2} \geq R \end{cases}. \quad (5)$$

These kinds of GRIN fibers have previously been proposed to simulate two-dimensional quantum oscillators [35].

For a fiber with transverse index  $\Delta n_{\text{GRIN}}$ , Eq. (2) is separable into radial  $\rho = \sqrt{x^2 + y^2}$  and polar  $\theta = \arctan(y/x)$  coordinates and the effective Hamiltonian has full  $O(2)$  rotational symmetry about the origin at  $\rho = 0$ . The lowest energy modes are approximately Laguerre-Gaussian modes centered at the origin; however, higher modes feel the boundary condition at  $\rho = R$ . The separability of (2) with  $\Delta n_{\text{GRIN}}$  means that all modes  $|\ell, n_\rho\rangle$  can be indexed by two modal indices, a radial modal number  $n_\rho = 0, 1, \dots$  and an azimuthal number  $\ell = 0, \pm 1, \pm 2, \dots$ . The index  $\ell$  is the quantum number for the  $O(2)$  symmetry. It represents the orbital angular momentum (OAM) and gives the charge of the central singularity. The other quantum number  $n_\rho$  gives the number of radial nodes.

Next, we section the fiber longitudinally with thin slabs of metal. For later applications to three-particle systems,

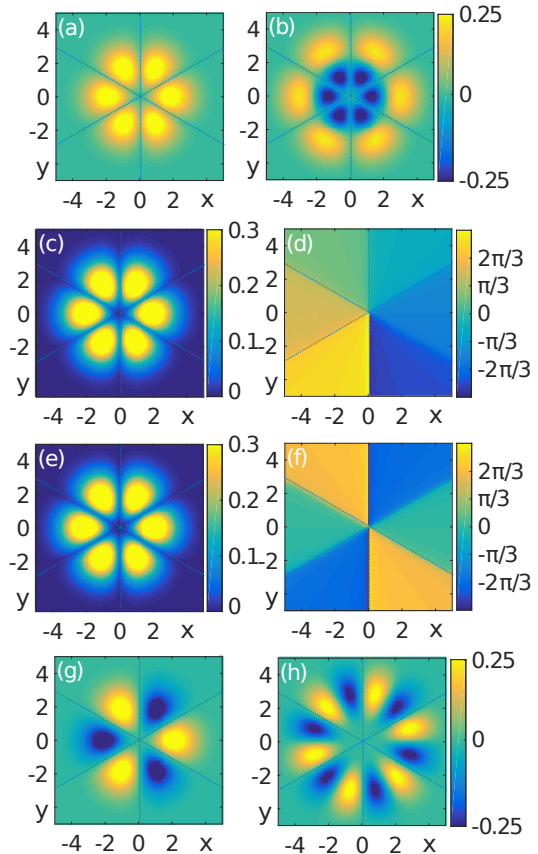


FIG. 3. Eigenfunctions for  $g = 10$ ,  $\sigma = 0.05$  and  $R \rightarrow \infty$ . (a) Ground state,  $|m, n_\rho, n_\theta\rangle = |0, 0, 0\rangle$ . (b) seventh state,  $|m, n_\rho, n_\theta\rangle = |0, 1, 0\rangle$ , which carries the first radial excitation of the ground state; (c) and (d) amplitude and phase of the vortex state  $|1, 0, 0\rangle$ ; (e) and (f) same for vortex state  $|2, 0, 0\rangle$ . (g) sixth excited state,  $|m, n_\rho, n_\theta\rangle = |3, 0, 0\rangle$ ; and (h) eighteenth state,  $|m, n_\rho, n_\theta\rangle = |3, 0, 1\rangle$ .

consider inserting three slabs that split the fiber into six identical sectors (see Fig. 1). This can be reasonably described by adding to  $\Delta n_{\text{GRIN}}$  an additional term formed by three Gaussians of width  $\sigma$ :

$$\Delta n_{C_{6v}}(x, y) = \frac{g}{\sigma\sqrt{2\pi}} \left\{ \exp\left[-\frac{x^2}{\sigma^2}\right] + \exp\left[-\frac{(x + \sqrt{3}y)^2}{4\sigma^2}\right] + \exp\left[-\frac{(x - \sqrt{3}y)^2}{4\sigma^2}\right] \right\}. \quad (6)$$

The function  $\Delta n_{C_{6v}}(x, y)$  has three maxima at the lines  $x = 0$  and  $x = \pm\sqrt{3}y$ , or equivalently at  $\theta \in \{\pi/6, \pi/2, 5\pi/6, 7\pi/6, 3\pi/3, 11\pi/6\}$ . This fiber profile therefore has  $C_{6v}$  symmetry, i.e. the six-fold dihedral symmetry of a snow flake, sometimes also denoted  $D_6$  or  $I_2(6)$ . More generally, if there are  $s$  bisecting metal slabs inserted evenly, then the system has  $C_{(2s)v}$  symmetry.

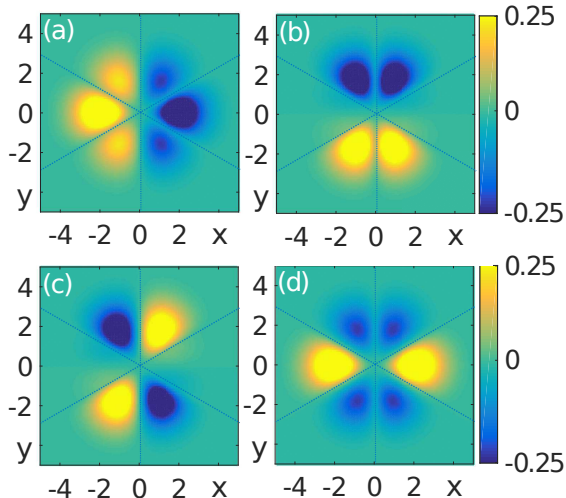


FIG. 4. Eigenfunctions for  $g = 10$  and  $\sigma = 0.05$ . (a) and (b), first excited doublet obtained combining the vortices with  $m = 1$  and  $m = -1$ , that is,  $|1, 0, 0\rangle \pm i|-1, 0, 0\rangle$ , respectively. (c) and (d), second excited doublet obtained as  $|2, 0, 0\rangle \pm i|-2, 0, 0\rangle$ , respectively.

The relationship between  $g$  in (6) and the optical parameters is crucial in the analogy discussed in section III. After recovering the spatial dimensions for  $\tilde{\sigma} = \sigma\lambda$ , one obtains

$$\frac{\Delta n_{C_{6v}}^{\max}(\lambda) \sqrt{2\pi\tilde{\sigma}}}{\lambda} = g. \quad (7)$$

In this work we are mainly interested in the limit where  $g$  is large. Because the left hand side of (7) includes only dimensional optical parameters, the large- $g$  limit can be reached experimentally with thin slabs of a metallic material of width  $\tilde{\sigma}$ , for which  $\Delta n_{C_{6v}}^{\max} = (n_0^2 - n_{\text{metal}}^2)/2n_0$ . For a perfect conductor,  $n_{\text{metal}}^2 \rightarrow -\infty$  and thus  $g$  is infinite. In an experimentally relevant case with a realistic metal, the dielectric constants have also an imaginary part, i.e.,  $\varepsilon = \varepsilon_1 + i\varepsilon_2$ . For example, for gold at  $\lambda = 1500\text{nm}$ , one has  $\varepsilon_1 = -106.94$  and  $\varepsilon_2 = 10.231$ . The losses due to the imaginary part are small for the limit in which  $g$  is large and  $\tilde{\sigma}$  small because the regions with large  $g$  have suppressed intensity, as we show later.

Combining the thin slabs of a metal with the GRIN fiber, the total refractive index is  $\Delta n_{\text{tot}} = \Delta n_{\text{GRIN}} + \Delta n_{C_{6v}}$ . The fiber has six identical symmetric domains  $\Omega_j$  ( $j \in \{1, \dots, 6\}$ ) where  $\Delta n_{\text{GRIN}}$  dominates separated by the thin barriers where  $\Delta n_{C_{6v}}$  dominates. The barriers break the  $O(2)$  rotational symmetry and as a result OAM  $\ell$  is no longer a good modal index. However, the discrete  $C_{6v}$  symmetry provides the possibility for alternate modal numbers based on the irreducible representations of  $C_{6v}$  [36, 37]; see appendix A for a summary. We choose the index called orbital angular pseudo-momentum (OAPM), introduced in the context of vortex

solitons [38, 39]. OAPM is a discrete index denoted  $m$  that identifies how the state transforms under a rotation by  $\pi/3$  and it gives the charge of the central singularity [40]. For example,  $m = 0$  means that there is no phase change from sector to sector and  $m = 3$  means the phase flips from sector to sector. Generally, the sectors differ by a complex phase  $\exp(im\pi/3)$  under counterclockwise rotation. When the analogy to the one-dimensional, three-body system is made in the next section, the OAPM will correlate to the particle content, i.e., we will show that  $m = 0$  corresponds to three identical bosons and  $m = 3$  to three identical fermions.

In the limit of narrow, impenetrable barriers,  $\tilde{\sigma} \rightarrow 0$  and  $g \rightarrow \infty$ , there are two additional modal numbers. Within each sector, there is approximate radial and polar separability and the number of radial nodes  $n_\rho$  and the number of azimuthal nodes *within a sector*  $n_\theta$  become effective descriptions. In this approximation, good labels for the modes are  $|m, n_\rho, n_\theta\rangle$ , where the first modal number  $m$ , is the OAPM which gives the phase relation among the sectors and the second two indices  $\{n_\rho, n_\theta\}$  give the mode structure within the sector. See appendix B for more details about the exact analytic solution in this limit.

To show how this works, we calculated numerically the eigenfunctions with finite interactions,  $g = 10$ , finite width,  $\sigma = 0.05$ , and  $R$  larger than the size of the computational domain (a box of side  $L = 10$ ). As shown in Fig. 2, in this limit the six modes with different  $m$  and same  $n_\rho$  and  $n_\theta$  are quasi-degenerate; In appendix B we show that they are exactly degenerate in the limit  $g \rightarrow \infty$  and  $\sigma \rightarrow 0$ . A selection of modes are depicted in Fig. 3, including (a) the ground state mode  $|0, 0, 0\rangle$ ; (b) the lowest energy state mode with one radial excitation  $|0, 1, 0\rangle$ ; and (h) the highest energy state mode with one polar excitation  $|3, 0, 1\rangle$ . Subfigures 3 (c)-(g) depict three other modes with  $n_\rho = 0$  and  $n_\theta = 0$ . We only depict  $m = 1$  and  $m = 2$  because the  $C_{6v}$  symmetry ensures that both modes with the  $|m| = 1$  and both modes with  $|m| = 2$  are degenerate. Because they are degenerate, instead of working with the complex modes  $|\pm 1, n_\rho, n_\theta\rangle$  and  $|\pm 2, n_\rho, n_\theta\rangle$  we can take linear combinations like  $|1, n_\rho, n_\theta\rangle \pm i|-1, n_\rho, n_\theta\rangle$  that result in real modes. Examples are presented in Fig. 4 that show that these real modes are no longer eigenstates of rotations, but they diagonalize into a pair of orthogonal reflections and have  $C_{2v}$  symmetry.

### III. OPTICAL ANALOGY TO THE THREE-PARTICLE MODEL

The fiber introduced in the previous section can simulate two-dimensional quantum systems, where the propagation modes become quantum states and are indexed by the OAPM, which is a conserved modal number. Indeed, all modal numbers can be understood as quantum numbers in this analogy. Despite their apparent

simplicity, two-dimensional quantum systems can display non-trivial behavior and the quantum dynamics can run the gamut from chaotic to superintegrable. In this section, we show how this fiber can be used to simulate a specific quantum system of current interest in ultracold atomic physics: three interacting atoms trapped in a one-dimensional harmonic potential with strong, short-range interactions (see e.g. the striking experiments in [41, 42]). We show that the optical modes of the fiber can simulate the wave functions of energy eigenstates for any particle statistics, including single-species and multi-species fermions and bosons. The OAPM modal number plays the role of effective statistical parameter; additional details are provided in appendix A.

To establish that the fiber can simulate the three-body, one-dimensional system, first consider the quantum Hamiltonian for three particles in a one dimensional harmonic trap:

$$H_0 = \frac{\hbar\omega}{2} \sum_{i=1}^3 \left( -\frac{d^2}{dx_i^2} + x_i^2 \right). \quad (8)$$

For convenience, we have scaled all distances by the harmonic oscillator length  $a = \sqrt{\hbar/(m\omega)}$  and the coordinates  $x_i$  are the dimensionless positions of the three particles. We add two-body interactions to the trap Hamiltonian  $H_0$  that only depend on the distance between the pairs of particles:

$$H = H_0 + V_{\text{int}} = \frac{\hbar\omega}{2} \sum_{i=1}^3 \left( -\frac{d^2}{dx_i^2} + x_i^2 \right) + \sum_{i<j} V_{ij} (|x_i - x_j|). \quad (9)$$

Now we perform the Jacobi transformation from the particle positions coordinates to the normalized Jacobi coordinates

$$R = \frac{x_1 + x_2 + x_3}{3}, \quad x = \frac{x_1 - x_2}{\sqrt{2}} \\ \text{and } y = \frac{x_1 + x_2}{\sqrt{6}} - \sqrt{\frac{2}{3}}x_3, \quad (10)$$

where  $R$  is proportional to the center-of-mass and  $x$  and  $y$  are a specific but arbitrary choice for the orientation of three-body relative coordinates. With this, Hamiltonian (9) becomes  $H = H_{\text{cm}} + H_{\text{rel}}$ , with

$$H_{\text{cm}} = -\frac{\hbar\omega}{2} \frac{d^2}{dR^2} + \frac{\hbar\omega}{2} R^2, \quad (11a)$$

$$H_{\text{rel}} = -\frac{\hbar\omega}{2} \frac{d^2}{dx^2} - \frac{\hbar\omega}{2} \frac{d^2}{dy^2} + \frac{\hbar\omega}{2} (x^2 + y^2) + V_{\text{int}}(x, y), \quad (11b)$$

$$V_{\text{int}}(x, y) = V_{12}(\sqrt{2}|x|) + V_{13} \left( \frac{|x + \sqrt{3}y|}{\sqrt{2}} \right) \\ + V_{23} \left( \frac{|x - \sqrt{3}y|}{\sqrt{2}} \right). \quad (11c)$$

This transformation therefore separates out the trivial center-of-mass degree of freedom whose dynamics are described by the one-dimensional oscillator  $H_{\text{cm}}$ . The remaining two relative degrees of freedom are described by  $H_{\text{rel}}$ .

Taking  $V_{ij}$  as a narrow Gaussian

$$V_{ij}(z) = \frac{g}{\sigma\sqrt{2\pi}} \exp\left[-\frac{z^2}{2\sigma^2}\right] \quad (12)$$

we recover the effective Hamiltonian given by the fiber mode propagation equation of the previous section with  $\Delta n_{\text{tot}} = \Delta n_{\text{GRIN}} + \Delta n_{C_{6v}}$  and all the analysis of the previous section holds. In particular, because this potential has  $C_{6v}$  symmetry, OAPM  $m \in \{-2, -1, 0, 1, 2, 3\}$  is a good quantum number. Further, in the limit of narrow, impenetrable barriers, the modes  $|m, n_\rho, n_\theta\rangle$  described in the previous section become exact and all six states with the same  $n_\rho$  and  $n_\theta$  become six-fold degenerate; see appendix B.

Just like the metallic slabs section the fiber into six sectors, the two-body interactions section the  $(x, y)$  relative configuration space of three particles into six sectors. Each sector corresponds to the particles being in a specific order; see Fig. 5. In a model with distinguishable particles, the phase relation between different orderings of particles is unconstrained. In contrast, three identical bosons must be symmetric under a particle exchange and three identical fermions must be antisymmetric. As a result, sectors corresponding to different orders must have specific phase relations if they are to represent the solutions of identical particles.

Conveniently, the OAPM  $m$  that derives from the  $C_{6v}$  symmetry describes the relative phase  $\exp(im\pi/3)$  of wave functions in individual sectors. Therefore, OAPM  $m$  can be used as a kind of statistical parameter that accounts for identical particles [43]. The case of  $m = 0$  and no phase difference across sector boundaries is appropriate for states of three bosons, denoted BBB modes. The case of  $m = 3$  leads to a phase difference of  $\pi$  across sector boundaries (a change of sign) and is therefore appropriate for three-fermion FFF modes. The cases  $m = \pm 1$  and  $m = \pm 2$  correspond to complex phase differences between sectors, but modes with the same magnitude of OAPM  $|m|$  have the same energy. Within the two-dimensional degenerate subspaces with  $|m| = 1$  and  $|m| = 2$ , there are superpositions that describe states that are symmetric under exchanges of two particles, for example, particle 1 and particle 2, but have no fixed phase relation for an exchange of particle 3. We call this a BBX mode, because it can describe the state of two identical bosons and one distinguishable third particle. Similarly, there are FFX modes where the exchange sectors corresponding to two identical fermions is antisymmetric and the third particle is distinguishable. What distinguishes the  $|m| = 1$  and  $|m| = 2$  is parity under coordinate inversion;  $|m| = 1$  modes are odd and  $|m| = 2$  are even. More details on how to derive these results are provided in appendix A.

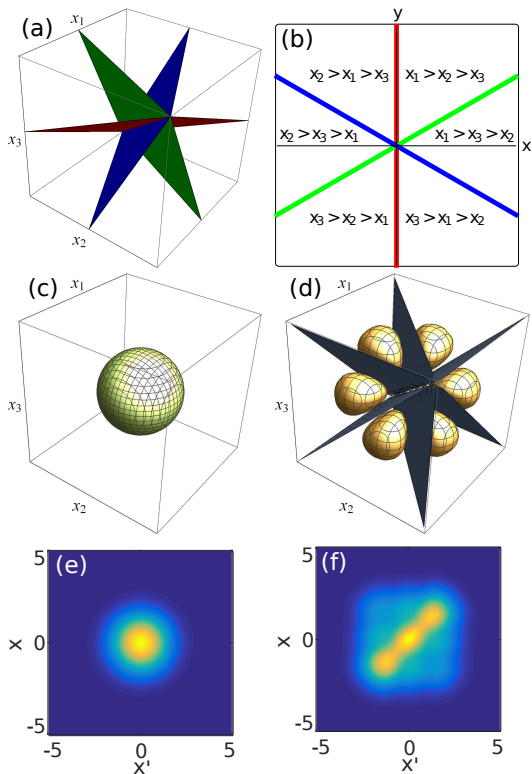


FIG. 5. (a) The full  $(x_1, x_2, x_3)$  three-particle configuration space. The three planes represent the two-body coincidences  $x_1 = x_2$  (red),  $x_2 = x_3$  (green) and  $x_3 = x_1$  (blue). (b) The relative  $(x, y)$  configuration space defined by the orthogonal Jacobi transformation (10). The lines are the projection of the planes in subfigure (a). Each of the six sectors corresponds to specific orderings of three particles. Reflecting across the two-particle coincidence lines is equivalent to a pairwise exchange of identical particles. Complete BBB wave function  $\Psi(x_1, x_2, x_3, z)$  for the non-interacting (c) and impenetrable delta-function barrier limits (d). (e) and (f) are the corresponding OBDM in each limit, respectively.

In light of this assignment of OAPM to possible combinations of identical particles, the mode level structure depicted in Fig. 2 reveals further insights. First, note because the phase of FFF modes must change sign at the section boundaries, the density must drop to zero and as a result FFF modes do not ‘feel’ the interaction strongly (or at all, in the impenetrable delta-function barrier limit). The energies of these  $m = 3$  FFF modes are therefore nearly horizontal even as the interaction strength  $g$  is increased. In contrast, the symmetric BBB modes experience the greatest variation with  $g$ , and in the large  $g$  converge to the same energy as an FFF mode with the same wave function in the sector (i.e. same  $n_\rho$  and  $n_\theta$ ), but alternating signs across sectors. This is an instance of the famous Bose-Fermi mapping for infinite strength contact interactions, first identified by Girardeau [44]; see Appendix C for more details. A generalized mapping also exists for the BBX and FFX states [45].

Proper illumination of the fiber permits appropriate

selection of the mode. For instance, to select a BBB mode one can simply illuminate with a Gaussian mode centered at the axis of symmetry. This has OAM  $\ell = 0$  and  $n_\rho = 0$ . This illumination will couple mostly to  $m = 0$ ,  $n_\rho = 0$  and  $n_\theta = 0$  and a small oscillation will occur due to the coupling to other modes within the same subspace, and thus same quantum numbers, except for  $n_\rho$ . We emphasize that it does not couple to any of the FFF modes or other modes with different  $m$  and  $n_\theta$  quantum numbers. To reduce this oscillation one can illuminate with a structured input beam, i.e., with a modulation of intensity that follows the  $C_{6v}$  symmetry of the BBB mode. To excite the FFF mode, one has to modulate not only the intensity but also to imprint a phase jump between sectors of  $\pi$ , as is commonly done with spatial phase modulators. For BBX or FFX modes with  $|m| = 1$  or 2, the input beam has to mimic the  $C_{2v}$  symmetry and the  $\pi$  phase jumps as in Fig. 4.

#### IV. INTERPRETATION OF THE OPTICAL MODE AMPLITUDE AS A MANY-BODY WAVE FUNCTION: CLASSICAL NON-SEPARABILITY

In this section we discuss how to extract the information on classical non-separability from the optical field at a certain distance  $z$ , which reads as  $\Phi(x, y, z)$ . To reconstruct the function in the  $(x_1, x_2, x_3)$  configuration space, one must account for the center of mass and its evolution along  $z$ . This is given by the modes of the one-dimensional harmonic oscillator, which we label with the quantum number  $n_R$ , and denote as  $\varphi_{n_R}(R)$ . So the total wave function is  $\Psi(x, y, R, z) = \Phi(x, y, z)\varphi_{n_R}(R)\exp[-in_R z]$ . From  $\Psi(x, y, R, z)$ , one transforms back to the variables  $(x_1, x_2, x_3)$  to get  $\Psi(x_1, x_2, x_3, z)$ . This procedure can be performed digitally after phase and amplitude detection of  $\Phi(x, y, z)$ .

With the total wave function  $\Psi(x_1, x_2, x_3, z)$ , one evaluates classical non-separability as follows. First, one calculates the one body density matrix (OBDM), defined as

$$\rho(x, x') = \int \Psi^*(x, x_2, x_3)\Psi(x', x_2, x_3)dx_2dx_3, \quad (13)$$

normalized to one. This operation can be performed digitally on a discrete matrix with techniques analogous to those used in digital image processing. To measure classical non-separability, one computes the von Neumann entropy,

$$S_{\rho(x, x')} = -\text{Tr}[\rho(x, x') \ln \rho(x, x')] = -\sum_j \lambda_j \ln \lambda_j. \quad (14)$$

where we denoted the eigenvalues of  $\rho(x, x')$  as  $\lambda_j$ . We recall that the von Neumann entropy is zero for a pure state (non-mixed) and maximal and equal to  $\ln(3)$  for a maximally mixed state (maximal non-separability).

Let us illustrate the interpretation of classical non-separability in this system with the three-boson case. In

such case, the ground state wave function for the non-interacting system is  $\Psi_{\text{B,gs}}(x_1, x_2, x_3) = C \left[ \prod_{i=1}^3 e^{-x_i^2/2} \right]$  with  $C$  a normalization constant; see Fig. 5 (c). In the impenetrable delta-function barrier limit, the wave function is

$$\phi_{\text{B,gs}}(x_1, x_2, x_3) = C \left[ \prod_{i=1}^3 e^{-x_i^2/2} \right] \prod_{1 \leq j < k \leq 3} |x_k - x_j|, \quad (15)$$

which is the solution obtained from the Bose-Fermi mapping theorem (see Fig. 5 (d) and appendix C). For the non-interacting case the von Neumann entropy is zero, and therefore separable. For the solution in the impenetrable delta-function barrier limit it is equal to  $S = 1.056$  which is close to the maximum,  $\ln(3) = 1.099$ , i.e., it is close to a maximally mixed state. In Fig. 5 (e) and (f) we represent the OBDM in both cases, which will help interpret what a mixed state means in this system. The diagonal of the OBDM (when  $x = x'$ ) is the probability of finding a particle at position  $x$ . For the non-interacting case, it is Gaussian, as corresponds to a single particle in a one-dimensional parabolic trap. When the interactions increase, this diagonal changes (see its computation for increasing  $g$  in [43]) and the states start to get mixed. This reflects the fact that the particles interact with each other. For the impenetrable delta-function barrier limit, two particles cannot occupy the same position along  $x$ . In such a case, if a particle is found at the center of the trap, the other two have to be slightly displaced to the edges. This explains the three-peak shape of the diagonal of the OBDM, while the appearance of structure in the off-diagonal terms highlights the presence of correlations in the system. This obviously means that, to determine the position of one particle, information about the position of the other particles is necessary. In the non-interacting case it was not necessary. This is the essence of classical non-separability in this system.

## V. CONCLUDING REMARKS

We introduced a new kind of optical fiber with a GRIN refractive index profile and three thin slabs of a metallic material. We classified the optical modes in such a fiber with appropriate modal numbers, and obtained exact solutions for the case in which the slabs are infinitely narrow and high. We showed that this fiber is the optical analogue of a quantum system of three atoms interacting with contact (delta-like) interactions confined in a one-dimensional trap. The modal numbers turn into quantum numbers through this analogy. In particular, the

modal number orbital angular pseudo-momentum plays the role of a statistical number, i.e., distinguishes among systems of three bosons, three fermions, or mixtures of two bosons or fermions plus a distinguishable particle. We showed that the spatial profile of the input beam permits to select the statistics of the atoms emulated in the fiber (e.g. three fermions, three fermions or mixtures).

We also proved that classical non-separability occurs in the system, as the optical modes (wave functions of energy eigenstates) in the limit where the slabs are infinitely narrow and high are close to maximally mixed states. Moreover, this is type (i) intersystem entanglement [9, 10, 12, 15], as it is not single particle but multi-particle entanglement. We remark that nonlocality may also be explored in such a setup through the Wigner representation of the state [46–48].

The analogy between optical and quantum systems allows us to infer novel mode structures in the optical systems, and this may inspire technological applications. For example, there are proposals for implementations of quantum computing algorithms in optical systems [35, 49, 50], optical implementations of teleportation protocols [51], and applications of the presence of classical non-separability for metrology [52, 53]. On top of this other properties defined only for the quantum system has been found in the classical ones, such as analogous to quantum (wave) chaos [54], quantum walks [55], or classical non-separability in vectorial vortex beams [56]. We expect that the system introduced here allows for the exploration of this kind of applications, especially when combined with polarization.

## FUNDING

Spanish Ministry MINECO (National Plan15 Grant: FISICATEAMO No. FIS2016-79508-P, SEVERO OCHOA No. SEV-2015-0522, FPI); European Social Fund; Fundació Cellex; Generalitat de Catalunya (AGAUR Grant No.2017, SGR 1341, and CERCA Program); European Commission (ERC AdG OSYRIS, EU FET-PRO QUIC); National Science Centre, Poland-Symfonia (Grant No. 2016/20/W/ST4/00314); TF acknowledges support under JSPS KAKENHI-18K13507, TB and TF acknowledge support from the Okinawa Institute of Science and Technology Graduate University.

## ACKNOWLEDGMENTS

We thank P. Grzybowski and E. Pisanty for encouraging and motivating discussions.

[1] P. Pesic, *Music and the Making of Modern Science* (MIT Press, 2014).

[2] R. Fedele and M. A. Man'ko, Eur. Phys. J. D **27**, 263 (2003).

- [3] M. A. Man'ko, *J. Phys.: Conf. Ser.* **99**, 012012 (2008).
- [4] S. Mukherjee, M. Valiente, N. Goldman, A. Spracklen, E. Andersson, P. Öhberg, and R. R. Thomson, *Phys. Rev. A* **94**, 053853 (2016).
- [5] D. Dragoman and M. Dragoman, *Quantum-Classical Analogies*, first edition ed. (Springer-Verlag Berlin Heidelberg, 2004).
- [6] G. Nienhuis and L. Allen, *Phys. Rev. A* **48**, 656 (1993).
- [7] S. Chávez-Cerda, J. R. Moya-Cessa, and H. M. Moya-Cessa, *J. Opt. Soc. Am. B*, *JOSAB* **24**, 404 (2007).
- [8] S. Longhi, *Laser & Photonics Reviews* **3**, 243 (2008).
- [9] R. J. C. Spreeuw, *Foundations of Physics* **28**, 361 (1998).
- [10] R. J. C. Spreeuw, *Phys. Rev. A* **63**, 062302 (2001).
- [11] P. Ghose and A. Mukherjee, *Reviews in Theoretical Science* **2**, 274 (2014).
- [12] A. Aiello, F. Töppel, C. Marquardt, E. Giacobino, and G. Leuchs, *New J. Phys.* **17**, 043024 (2015).
- [13] A. Luis, *Optics Communications* **282**, 3665 (2009).
- [14] E. Karimi and R. W. Boyd, *Science* **350**, 1172 (2015).
- [15] N. L. Harshman and S. Wickramasekara, *Open Syst Inf Dyn* **14**, 341 (2007).
- [16] W. F. Balthazar, C. E. R. Souza, D. P. Caetano, E. F. G. ao, J. A. O. Huguenin, and A. Z. Khoury, *Opt. Lett.* **41**, 5797 (2016).
- [17] K. F. Lee and J. E. Thomas, *Phys. Rev. Lett.* **88**, 097902 (2002).
- [18] J. Fu, Z. Si, S. Tang, and J. Deng, *Phys. Rev. A* **70**, 042313 (2004).
- [19] K. F. Lee and J. E. Thomas, *Phys. Rev. A* **69**, 052311 (2004).
- [20] F. D. Zela, *Optica* **5**, 243 (2018).
- [21] B. Stoklasa, L. Motka, J. Rehacek, Z. Hradil, L. L. Snchez-Soto, and G. S. Agarwal, *New Journal of Physics* **17**, 113046 (2015).
- [22] X.-F. Qian, B. Little, J. C. Howell, and J. H. Eberly, *Optica* **2**, 611 (2015).
- [23] D. Gloge and E. A. J. Marcatili, *Bell System Technical Journal* **52**, 1563 (1973).
- [24] A. Ghatak and M. S. Sodha, *Inhomogeneous Optical Waveguides (Optical Physics and Engineering)* (Springer, New York, 1977) pp. x, 269.
- [25] A. W. Snyder and J. D. Love, *Optical waveguide theory*, Vol. Science paperbacks ; 190 (Chapman and Hall, London ; New York, 1983).
- [26] S. Longhi, *Opt. Lett.* **28**, 2363 (2003).
- [27] A. Mafi, *Journal of Lightwave Technology* **30**, 2803 (2012).
- [28] W. Renninger and F. Wise, *Nature Communications* **4**, 1719 (2013).
- [29] L. G. Wright, D. N. Christodoulides, and F. W. Wise, *Nature Photonics* **9**, 306 (2015).
- [30] L. G. Wright, Z. Liu, D. A. Nolan, M.-J. Li, D. N. Christodoulides, and F. W. Wise, *Nature Photonics* **10**, 771 (2016).
- [31] K. Krupa, A. Tonello, B. M. Shalaby, M. Fabert, A. Barthélémy, G. Millot, S. Wabnitz, and V. Couderc, *Nature Photonics* **11**, 237 (2017).
- [32] M. Conforti, C. Mas Arabi, A. Mussot, and A. Kudlinski, *Optics Letters* **42**, 4004 (2017).
- [33] S. G. Krivoshlykov and I. N. Sissakian, *Opt Quant Electron* **12**, 463 (1980).
- [34] S. K. Joseph, J. Sabuco, L. Y. Chew, and M. A. F. Sanjuán, *Opt. Express*, *OE* **23**, 32191 (2015).
- [35] M. A. Man'ko, V. I. Man'ko, and R. Vilela Mendes, *Physics Letters A* **288**, 132 (2001).
- [36] P. McIsaac, *IEEE Transactions on Microwave Theory and Techniques* **23**, 421 (1975).
- [37] R. Guobin, W. Zhi, L. Shuqin, and J. Shuisheng, *Opt. Express*, *OE* **11**, 1310 (2003).
- [38] A. Ferrando, *Phys. Rev. E* **72**, 036612 (2005).
- [39] M. Á. García-March, A. Ferrando, M. Zacarés, J. Vi-jande, and L. D. Carr, *Physica D: Nonlinear Phenomena Nonlinear Phenomena in Degenerate Quantum Gases*, **238**, 1432 (2009).
- [40] M.-Á. García-March, A. Ferrando, M. Zacarés, S. Sahu, and D. E. Ceballos-Herrera, *Phys. Rev. A* **79**, 053820 (2009).
- [41] F. Serwane, G. Zürn, T. Lompe, T. B. Ottenstein, A. N. Wenz, and S. Jochim, *Science* **332**, 336 (2011).
- [42] A. N. Wenz, G. Zürn, S. Murmann, I. Brouzos, T. Lompe, and S. Jochim, *Science* **342**, 457 (2013).
- [43] M. A. García-March, B. Juliá-Díaz, G. E. Astrakharchik, J. Boronat, and A. Polls, *Phys. Rev. A* **90**, 063605 (2014).
- [44] M. Girardeau, *Journal of Mathematical Physics* **1**, 516 (1960).
- [45] N. L. Harshman, *Few-Body Syst* **57**, 11 (2016).
- [46] K. Banaszek and K. Wódkiewicz, *Phys. Rev. A* **58**, 4345 (1998).
- [47] T. Fogarty, T. Busch, J. Goold, and M. Paternostro, *New Journal of Physics* **13**, 023016 (2011).
- [48] J. Li, T. Fogarty, C. Cormick, J. Goold, T. Busch, and M. Paternostro, *Phys. Rev. A* **84**, 022321 (2011).
- [49] N. Bhattacharya, H. B. van Linden van den Heuvell, and R. J. C. Spreeuw, *Phys. Rev. Lett.* **88**, 137901 (2002).
- [50] B. Perez-Garcia, J. Francis, M. McLaren, R. I. Hernandez-Aranda, A. Forbes, and T. Konrad, *Physics Letters A* **379**, 1675 (2015).
- [51] D. Guzman-Silva, R. Brning, F. Zimmermann, C. Vetter, M. Grfe, M. Heinrich, S. Nolte, M. Duparr, A. Aiello, M. Ornigotti, and A. Szameit, *Laser & Photonics Reviews* **10**, 317 (2016).
- [52] F. Toepfel, A. Aiello, C. Marquardt, E. Giacobino, and G. Leuchs, *New Journal of Physics* **16**, 073019 (2014).
- [53] S. Berg-Johansen, F. Töppel, B. Stiller, P. Banzer, M. Ornigotti, E. Giacobino, G. Leuchs, A. Aiello, and C. Marquardt, *Optica* **2**, 864 (2015).
- [54] V. Doya, O. Legrand, F. Mortessagne, and C. Miniatura, *Phys. Rev. E* **65**, 056223 (2002).
- [55] P. L. Knight, E. Roldán, and J. E. Sipe, *Phys. Rev. A* **68**, 020301 (2003).
- [56] V. D'Ambrosio, G. Carvacho, F. Graffitti, C. Vitelli, B. Piccirillo, L. Marrucci, and F. Sciarrino, *Phys. Rev. A* **94**, 030304 (2016).
- [57] N. L. Harshman, *Phys. Rev. A* **86**, 052122 (2012).
- [58] M. Hamermesh, *Group Theory and Its Application to Physical Problems*, reprint edition ed. (Dover Publications, New York, 1989).
- [59] L. D. Landau and E. M. Lifshitz, in *Quantum Mechanics (Third Edition)* (Pergamon, 1977) third edition ed., pp. 50 – 81.
- [60] M. E. S. Andersen, N. L. Harshman, and N. T. Zinner, *Phys. Rev. A* **96**, 033616 (2017).

## Appendix A: Classification of mode symmetries

For any form of two-body interaction and a harmonic trap, the three-particle Hamiltonian (9) is symmetric under the finite group of transformations given by the particle permutation symmetry of three identical (but not necessarily indistinguishable) particles combined with parity inversion about the minimum of the harmonic trapping potential. When these symmetries are restricted to relative configuration space, they realize the point group  $C_{6v}$ , i.e. the rotation and reflection symmetries of a hexagon [45, 57]. The twelve elements of  $C_{6v}$  and their realizations as transformations of relative configuration space are summarized in Table I. An optical fiber simulating the three-body particle model will have this hexagonal symmetry in the transverse profile of the fiber.

Subgroups of  $C_{6v}$  are useful when the particles are partially distinguishable. We call attention to three subgroups in particular:

- The group generated by reflections across the three lines  $x = 0$ ,  $x + \sqrt{3}y = 0$ , and  $x - \sqrt{3}y = 0$  is a subgroup of  $C_{6v}$  isomorphic to  $C_{3v}$ , the symmetry of an equilateral triangle. This group has six elements and is the realization in the fiber of the permutation symmetry of three identical particles. Each reflection corresponds to a pairwise particle exchange. For example, the reflection across the line  $x = 0$  in the fiber corresponds to exchanging particles 1 and 2 in the particle model. The two rotations by  $2\pi/3$  correspond to cyclic three-particle exchanges in the model.
- The subgroup containing only the rotations in  $C_{6v}$  is called  $C_6$ . This group is useful for the analysis of vortex states of light because the generator of  $C_6$  is rotation by  $\pi/3$  and a state with OAPM  $m$  transforms like  $\exp(im\pi/3)$  under this rotation.
- There are several subgroups of  $C_{6v}$  that are isomorphic to  $C_{2v}$ , i.e. the point symmetries of a rectangle. In particular, we focus on the instance of  $C_{2v}$  that aligns with the  $\{x, y\}$  Jacobi coordinates and includes the reflection corresponding to the exchange of particle 1 and 2. This subgroup is useful when considering the case of partially distinguishable particles like two bosons in the same spin state and one distinguishable by a different spin state. It also applied when one of the two-body interactions is different from the other two.

Because  $C_{6v}$  is a symmetry of the fiber and the relative interacting Hamiltonian, energy levels are associated to its irreducible representations (irreps), whose properties are summarized in Table II. There are four one-dimensional (or singlet) irreps denoted  $A_1$ ,  $A_2$ ,  $B_1$  and  $B_2$  and two two-dimensional (or doublet) irreps denoted  $E_1$  and  $E_2$ . This means that unless some other symmetry is present, there will only be singly-degenerate or

$g \in C_{6v}$	$g \in S_3 \times Z_2$	$\varphi \rightarrow \varphi'$
$E$	$\hat{e}$	$\varphi$
$\sigma_v$	$\hat{\sigma}_{12}$	$-\varphi + \pi$
$\sigma_{v'}$	$\hat{\sigma}_{23}$	$-\varphi + \frac{\pi}{3}$
$\sigma_{v''}$	$\hat{\sigma}_{31}$	$-\varphi - \frac{\pi}{3}$
$C_3^{-1}$	$\hat{\sigma}_{231}$	$\varphi - \frac{2\pi}{3}$
$C_3$	$\hat{\sigma}_{312}$	$\varphi + \frac{2\pi}{3}$
$C_2$	$\hat{\pi}$	$\varphi + \pi$
$\sigma_d$	$\hat{\pi}\hat{\sigma}_{12}$	$-\varphi$
$\sigma_{d'}$	$\hat{\pi}\hat{\sigma}_{23}$	$-\varphi - \frac{2\pi}{3}$
$\sigma_{d''}$	$\hat{\pi}\hat{\sigma}_{31}$	$-\varphi + \frac{2\pi}{3}$
$C_6$	$\hat{\pi}\hat{\sigma}_{231}$	$\varphi + \frac{\pi}{3}$
$C_6^{-1}$	$\hat{\pi}\hat{\sigma}_{312}$	$\varphi - \frac{\pi}{3}$

TABLE I. The first column is the symmetry transformation designated by the corresponding element of the point symmetry group of the regular hexagon permutation group  $C_{6v}$ . The second column is the same transformation expressed as the corresponding element of  $S_3 \times Z_2$ . We use the notation for  $S_3$  permutation group elements such that  $e$  is the identity, the 2-cycle  $\hat{\sigma}_{ij}$  switches particles  $i$  and  $j$ , and 3-cycle  $\hat{\sigma}_{ijk}$  switches 1 to  $i$ , 2 to  $j$  and 3 to  $k$ . The element  $\hat{\pi}$  is parity inversion. The third column is the rotation or reflection matrix in Jacobi cartesian coordinates  $\{x, y\}$ , and the fourth column is the equivalent transformation of the cylindrical Jacobi coordinate  $\tan \varphi = y/x$ .

doubly-degenerate energy levels, as is demonstrated by our numerical solutions, see Fig. 2. Note that half of the irreps correspond to even parity states and half to odd parity states. We plot in Fig. 3 two examples of XYZ solutions, these are very important *vortex*-like solutions.

$C_{6v}$	$[C_{3v}]^\pi$	$C_6$	$C_{2v}$	Possibilities
$A_1$	$[3]^+$	$m = 0$	$A_1$	BBB, BBX, XYZ
$A_2$	$[1^3]^+$	$m = 3$	$A_2$	FFF, FFX, XYZ
$B_1$	$[1^3]^-$	$m = 3$	$B_1$	FFF, FFX, XYZ
$B_2$	$[3]^-$	$m = 0$	$B_2$	BBB, BBX, XYZ
$E_1$	$[21]^-$	$m =  1 $	$B_1$ $B_2$	FFX, XYZ BBX, XYZ
$E_2$	$[21]^+$	$m =  2 $	$A_1$ $A_2$	BBX, XYZ FFX, XYZ

TABLE II. The first column lists the irreps of  $C_{6v}$  using the notation of [58]. The second column shows how irreps of  $C_{6v}$  can also be described as irreps of  $C_{3v}$  and parity. The group  $C_{3v}$  is isomorphic to the symmetric group  $S_3$  and has a totally symmetric irrep denoted  $[3]$ , a totally antisymmetric irrep denoted  $[1^3]$  and a mixed symmetry irrep denoted  $[21]$ . The third column lists the OAPM that characterize the irreps of  $C_6$ . The fourth column give the irreps of  $C_{2v}$ ; for the two-dimensional  $C_{6v}$  irreps  $E_1$  and  $E_2$  there are two irreps of  $C_6$  and  $C_{2v}$  that appear, and they can be thought of as different ways of diagonalizing the doublet. The final column gives the possible particle content of each state. BBB (FFF) means three indistinguishable bosons (fermions); BBX (FFX) two indistinguishable bosons (fermions) and one other identical but distinguishable particle; XYZ three identical but distinguishable particles.

Distinguishable identical particles do not necessarily have any specific particle exchange symmetry, so they

can populate any type of irrep. Indistinguishable bosons must be symmetric under pairwise exchanges and can only populate energy levels that carry the singlet irreps  $A_1$  (positive parity) and  $B_2$  (negative parity). Indistinguishable fermions must be antisymmetric, and can only populate  $A_2$  (positive parity) and  $B_2$  (negative parity) energy levels. Partially distinguishable bosons and fermions are more complicated. For example, two indistinguishable bosons and a third particle must be symmetric under the exchange of two of the particles, say particles 1 and 2, but can have any symmetry relation with the third. As a result, they effectively have  $C_{2v}$  symmetry and should be in a bosonic irrep of that subgroup. See Table II for a cataloging of these results.

The  $C_{6v}$  symmetry is independent of the strength and exact form of the two-body interaction, and this has consequences for adiabatic or diabatic changes in the Hamiltonian. When the Hamiltonian changes, there can at most be mixing between energy levels carrying the same irrep. Therefore, the symmetry of the input beam determines which irreps, and therefore, the effective particle content of the interacting model being simulated.

## Appendix B: Exact solutions of approximate models

The solutions of (2) with  $\Delta n_{\text{tot}} = \Delta n_{\text{GRIN}} + \Delta n_{C_{6v}}$  are exactly solvable in two limits:  $g \rightarrow 0$  corresponding to no metallic slabs and  $\tilde{\sigma} \rightarrow 0$  together with  $g \rightarrow \infty$  corresponding to narrow, impenetrable barriers, aka infinite or impenetrable delta-barriers. These solutions allow us to interpret the numerical solutions in Figs. 2-4 and understand the approximate modal numbers of the states  $|m, n_\rho, n_\theta\rangle$ .

### 1. Potential given by GRIN fiber

First consider a fiber with transverse index  $\Delta n_{\text{GRIN}}$  and no metallic slabs. In the limit of large fibers, the boundary at  $\rho = R$  can be ignored for the lowest modes and the optical Schrödinger equation (4) describes a two-dimensional isotropic harmonic oscillator [6]. Note that because the center-of-mass separates, the Hamiltonian for the relative coordinates of three non-interacting equal-mass particles in a one-dimensional harmonic trap is also described by a two-dimensional harmonic oscillator.

The two-dimensional isotropic harmonic oscillator is separable in cartesian, polar and elliptic coordinates. Separating in polar coordinates, the modes indices correspond to orbital angular momentum (OAM)  $\ell = 0, \pm 1, \pm 2, \dots$  and the number of radial nodes  $n_\rho = 0, 1, \dots$ . The corresponding solutions for the mode functions in polar coordinates  $|\ell, n_\rho\rangle$  are given by

$$\phi_{\ell, n_\rho}(\rho, \theta) = N \rho^{|\ell|} L_{n_\rho}^{|\ell|}(\rho^2) e^{-\rho^2/2} e^{i\ell\theta}, \quad (\text{B1})$$

with  $L_{n_\rho}^{|\ell|}(z)$  the generalized Laguerre polynomial and normalization constant  $N = n_\rho!/\pi(n_\rho + |\ell|)!$ . These modes (B1) correspond to Laguerre-Gaussian modes centered at the origin with OAM given by  $\ell$ . The propagation constant (analogous to energy) of the mode  $|\ell, n_\rho\rangle$  is  $\mu = 2n_\rho + |\ell| + 1$  and except for the lowest mode  $|\ell, n_\rho\rangle = |0, 0\rangle$ , all modes are degenerate with degeneracy  $N(\mu) = \mu$ .

### 2. GRIN and infinite delta-barriers

Inserting the metal slabs breaks the rotational symmetry, so OAM  $\ell$  is no longer a meaningful quantum number because for slabs with finite width and finite strength, the system is no longer separable in polar coordinates (or any other coordinates) and does not have exact solutions. However, in this section we show that in the infinite delta-barrier limit the modes  $|m, n_\rho, n_\theta\rangle$  labeled by the OAPM  $m$ , the number of polar nodes  $n_\theta$  per sector and the number of radial nodes  $n_\rho$  per sector become exact solutions.

In the limit of infinitely narrow slabs  $\tilde{\sigma} \rightarrow 0$ , the Gaussian profiles in (6) tend to delta functions, so it can be approximated as

$$\begin{aligned} \Delta n_{C_{6v}}(x, y) &\approx g \left[ \delta(x) + \sqrt{2}\delta(x + \sqrt{3}y) + \sqrt{2}\delta(x - \sqrt{3}y) \right] \\ &= \frac{g}{\rho} \sum_{j=1}^6 \delta\left(\theta - \frac{2j-1}{6}\right). \end{aligned} \quad (\text{B2})$$

Note that the apparent singularity at  $\rho = 0$  is not strong enough to disrupt the self-adjointness of the effective Hamiltonian and there is no danger of “falling to the center” [59]. Even in this limit (B2), the potential  $\Delta n_{C_{6v}}(x, y)$  does not have the necessary functional form  $f(\theta)/\rho^2$  for the mode equation to separate in polar coordinates unless the simultaneous limit  $g \rightarrow \infty$  is taken. Only in this impenetrable limit does the separability return and the modes  $|m, n_\rho, n_\theta\rangle$  correspond to exact solutions.

To understand how this works in the idealized limit of infinite  $\delta$ -barriers [see (B2)], we note that each of the identical six sectors of the fiber are dynamically independent. Therefore, the mode equation (2) separates in polar coordinates and the numbers  $n_\rho$  and  $n_\theta$  become good modal numbers again. For example, the solution in the sector  $\Omega_1 = [-\pi/6, \pi/6]$  (arbitrarily denoted the first sector and labeled by  $j = 1$ ) is

$$\phi_{n_\rho, n_\theta}^1(\rho, \theta) = N \rho^{n_\theta} L_{n_\rho}^{n_\theta}(\rho^2) \exp[-\rho^2/2] \sin[3(n_\theta+1)(\theta+\pi/6)]. \quad (\text{B3})$$

This equation satisfies the optical Schrödinger equation for a GRIN fiber (i.e., it is a special case of (B1)) and also satisfies the nodal boundary condition at the sectioning metal slabs when  $n_\rho$  and  $n_\theta$  are non-negative integers. By analogy with (B1) or by direct calculation, one shows the propagation constant of this mode is  $\mu = 2n_\rho + 3n_\theta + 4$ .

To get the mode solutions in the whole fiber, six of these section functions with the same  $n_\rho$  and  $n_\theta$  are pasted together with phase relationships across the metal slabs given by the OAPM  $m$

$$\phi_{m,n_\rho,n_\theta}(\rho,\theta) = \phi_{n_\rho,n_\theta}^1(\rho,\theta - \theta_j) \exp[-im\theta_j] \text{ for } \theta \in \Omega_j \quad (\text{B4})$$

where  $\theta_j = (j-1)\pi/3$  and  $\Omega_j = [(2j-3)\pi/6, (2j-1)\pi/6]$ . There are only six ways to choose the relative phases and paste the section functions together such that the state respects  $C_{6v}$  symmetry, and for these six possibilities the OAPM  $m$  takes the values  $m = 0, \pm 1, \pm 2$  and  $3$ . As detailed in appendix A, the OAPM describes how the state transforms under the symmetry transformation in  $C_{6v}$  and how this symmetry connects with the particle content of the analogous interacting three-particle model.

The six states  $|m, n_\rho, n_\theta\rangle$  with the same  $n_\rho$  and  $n_\theta$  are degenerate and have the same propagation constant  $\mu = 2n_\rho + 3n_\theta + 4$  independent of OAPM  $m$ . In this limit, the effective Hamiltonian is superintegrable, i.e. there are more integrals of motion than degrees of freedom [60]. This degeneracy is only present in the idealized case of  $\delta$  barriers and infinite  $g$ . For both the idealized finite- $g$   $\delta$  barrier potential (B2) and the more realistic Gaussian potential (6), the tunneling among sectors lifts the degeneracy so that states with different  $|m|$  have different propagation constants.

### Appendix C: Bose-Fermi mapping

The exact solutions for three bosons in a harmonic trap in the infinite delta-barrier limit (B2) can also be derived from the Bose-Fermi mapping [44], which we describe here briefly.

The non-interacting Hamiltonian (8) is a three-dimensional isotropic harmonic oscillator and can be exactly solved in many different coordinate systems. Perhaps the most obvious is the product single-particle wave functions

$$\phi_{n_1,n_2,n_3}(x_1,x_2,x_3) = \varphi_{n_1}(x_1)\varphi_{n_2}(x_2)\varphi_{n_3}(x_3) \quad (\text{C1})$$

where  $\varphi_n(x)$  is the one-dimensional harmonic oscillator energy eigenstate

$$\varphi_n(x) = \left(\pi^{1/4}\sqrt{2^n n!}\right)^{-1} e^{-x^2/2} H_n(x) \quad (\text{C2})$$

with energy  $\hbar\omega(n + 1/2)$  ( $H_n(x)$  is the  $n$ th Hermite polynomial). Therefore, the state (C1) has total energy  $E = \hbar\omega(n_1 + n_2 + n_3 + 3/2)$ .

For distinguishable particles, the quantum numbers  $n_i$  can take any non-negative integer value, but for identical (or partially identical) sets of fermions or bosons, then there are restrictions on the sets of allowed  $n_i$  and the states (C1) must be symmetrized and antisymmetrized appropriately. The ground state for three identical non-interacting bosons is the state  $\{n_1, n_2, n_3\} = \{0, 0, 0\}$  and

remains separable, but the first excited bosonic state is the symmetric combination of the three permutations of  $\{n_1, n_2, n_3\} = \{0, 0, 1\}$  and is not separable.

Similarly, the ground state of fermions is the antisymmetrized superposition of six permutations of the state (C1) with  $\{n_1, n_2, n_3\} = \{0, 1, 2\}$ , also known as the Slater determinant. In the ground state each fermion occupies one of the three lowest energy single-particle eigenstates, and thus the energy of the state is  $E = \hbar\omega(1/2 + 3/2 + 5/2) = 9/2\hbar\omega$ . A bit of algebra brings the antisymmetrized expression for the fermionic ground state into a Jastrow form

$$\phi_{\text{F,gs}}(x_1, x_2, x_3) = C \left[ \prod_{i=1}^3 e^{-x_i^2/2} \right] \prod_{1 \leq j < k \leq 3} (x_k - x_j), \quad (\text{C3})$$

with

$$C = 2^{3/2} \left(\frac{1}{a}\right)^{3/2} \left[ 3! \prod_{n=0}^2 n! \sqrt{\pi} \right]^{-1/2}. \quad (\text{C4})$$

Because of the the factor  $(x_k - x_j)$  for each pair of particles in (C3), the function  $\phi_{\text{F,gs}}(x_1, x_2, x_3)$  vanishes wherever two particles coincide and changes sign as one moves across this boundary, as one expects for antisymmetrized fermionic states (see Fig. 1). Excited fermion states  $\phi_{\text{F,exc}}(x_1, x_2, x_3)$  can be constructed either by using Slater determinants of states with set of three distinct quantum numbers higher in energy than  $\{0, 1, 2\}$  or, by analogy with (C3), finding higher-order totally antisymmetric polynomials of three variables.

Fermionic states have nodes whenever  $x_i = x_j$ , so they do not “feel” the  $\delta$ -function two-body interaction and therefore non-interacting fermionic energy eigenstates are also energy eigenstates of the Hamiltonian (9) in the limit when the interactions are zero-range. Some algebra demonstrates that when restricted to the relative coordinate, the ground state wave function (C3) has the same form as the eigenmode  $|m = 3, n_\rho = 0, n_\theta = 0\rangle$  and the first excited state constructed from the Slater determinant of  $\{0, 1, 3\}$  corresponds to  $|m = 3, n_\rho = 0, n_\theta = 1\rangle$ . After that the identification gets more complicated because of degeneracies.

The Bose-Fermi mapping theorem allows one to construct the exact solution for three interacting identical bosons with delta-barrier interactions and  $g \rightarrow \infty$  from the exact solution for non-interacting fermions [44]. This is easily fulfilled for the ground state taking the modulus of the solution,  $\phi_{\text{B,gs}} = |\phi_{\text{F,gs}}|$ , which gives rise to

$$\phi_{\text{B,gs}} = C \left[ \prod_{i=1}^3 e^{-x_i^2/2} \right] \prod_{1 \leq j < k \leq 3} |x_k - x_j|. \quad (\text{C5})$$

The excited bosonic states are obtained in the same way from those of the excited fermions by defining a symmetrization function  $A(x_1, x_2, x_3) = \prod_{j>i} \text{sign}(x_j - x_i)$ , with  $\text{sign}(x)$  the sign function to adjust the relative

phases. Then any excitation is obtained as  $\phi_{\text{B,exc}} = A\phi_{\text{F,exc}}$ . In the relative eigenmode basis  $|m, n_\rho, n_\theta\rangle$ , this mapping is equivalent to switching the OAPM from  $m = 3$  to  $m = 0$ .